Available online at www.sciencedirect.com

ScienceDirect

Acta Materialia 85 (2015) 216–228

Acta MATERIALIA

www.elsevier.com/locate/actamat

Nanolaminate transformation-induced plasticity–twinning-induced plasticity steel with dynamic strain partitioning and enhanced damage resistance

M.-M. Wang,[a] C.C. Tasan,[a,*] D. Ponge,[a] A.-Ch. Dippel[b] and D. Raabe[a]

[a] *Max-Planck-Institut für Eisenforschung, Max-Planck-Straße 1, 40237 Düsseldorf, Germany*
[b] *Deutsches Elektronen-Synchrotron DESY, Hamburg, Germany*

Received 9 May 2014; accepted 6 November 2014

Abstract—Conventional martensitic steels have limited ductility due to insufficient microstructural strain-hardening and damage resistance mechanisms. It was recently demonstrated that the ductility and toughness of martensitic steels can be improved without sacrificing the strength, via partial reversion of the martensite back to austenite. These improvements were attributed to the presence of the transformation-induced plasticity (TRIP) effect of the austenite phase, and the precipitation hardening (maraging) effect in the martensitic matrix. However, a full micromechanical understanding of this ductilizing effect requires a systematic investigation of the interplay between the two phases, with regards to the underlying deformation and damage micromechanisms. For this purpose, in this work, a Fe–9Mn–3Ni–1.4Al–0.01C (mass%) medium-Mn TRIP maraging steel is produced and heat-treated under different reversion conditions to introduce well-controlled variations in the austenite–martensite nanolaminate microstructure. Uniaxial tension and impact tests are carried out and the microstructure is characterized using scanning and transmission electron microscopy based techniques and post mortem synchrotron X-ray diffraction analysis. The results reveal that (i) the strain partitioning between austenite and martensite is governed by a highly dynamical interplay of dislocation slip, deformation-induced phase transformation (i.e. causing the TRIP effect) and mechanical twinning (i.e. causing the twinning-induced plasticity effect); and (ii) the nanolaminate microstructure morphology leads to enhanced damage resistance. The presence of both effects results in enhanced strain-hardening capacity and damage resistance, and hence the enhanced ductility.

Keywords: Reverted austenite; TRIP-maraging; Strain partitioning; TWIP; Damage

1. Introduction

Martensitic steels exhibit high strength but low ductility due to lack of effective hardening and microcrack-arresting mechanisms [1–3]. It has thus been a permanent challenge to improve the ductility of martensitic steels, without sacrificing strength. Different approaches have been explored, focusing on prior austenite state in terms of chemical composition [4–6], grain size [7,8]; defect density [9,10]; tempering of martensite [11,12]; martensite variant selection [13–16]; martensite refinement [4,17,18]; multilayering [19–22], etc. For the same purpose, we have recently introduced a novel alloy and microstructure design concept which we refer to as transformation-induced plasticity (TRIP)-maraging steels [23,24]. In this concept the microstructure is designed in two ways in a single aging treatment step: reverted nanoscale austenite films (γ_{RN}) are formed on the martensite interfaces and nanoparticles are precipitated in the martensitic matrix [25]. In this way these steels benefit from three effects simultaneously, i.e. the TRIP effect [26–30] (from the former), the maraging effect (through the latter) [31], and the classical composite effect. A simultaneous increase in both ductility and strength has already been demonstrated, providing indirect verification of the successful introduction of effective hardening and microcrack-arresting mechanisms in the martensitic matrix through this concept [23,25]. The exact nature of the aging-induced improvements is, however, not fully understood, especially considering the complexity of microstructure optimization required. In this regard, improper chemical composition or thermomechanical treatment considerations may lead to the introduction of additional damage mechanisms (e.g. due to the strain incompatibility of hard (martensite) and soft (γ_{RN}) phases introduced) or ineffective TRIP contribution (e.g. spent early in deformation and absent when needed for damage resistance at high-strain levels).

Therefore in this work, in an effort to provide generalized guidelines for martensitic steel design, we aim to obtain a thorough understanding of the micromechanical processes governing TRIP-maraging steel behavior, i.e. martensite and γ_{RN} plasticity, deformation-induced γ_{RN} transformation and the nucleation and microstructure interaction of damage incidents. For this purpose, employing advanced experimental multiprobe and in situ techniques, (i) the microstructure development in TRIP-maraging steels during austenite reversion process, (ii) the resulting mechanical properties and (iii) microstructural deformation

* Corresponding author. Tel.: +49 2116792866; e-mail: c.tasan@mpie.de

http://dx.doi.org/10.1016/j.actamat.2014.11.010
1359-6462/

and damage mechanisms are systematically studied. In what follows, we first explain this employed experimental multiprobe methodology. Then the microstructure evolution during martensite-to-austenite reversion and its influence on the overall mechanical properties are analyzed. Next, the deformation, damage and failure micromechanisms responsible for the observed mechanical trends are studied in detail, through a variety of both in situ and post mortem measurements. Finally the observations are discussed in comparison to other advanced high strength steels with multiphase microstructures.

2. Experimental procedure

The study was carried out on a TRIP-maraging steel with nominal chemical composition Fe–9Mn–3Ni–1.4Al–0.01C (mass%). Mn thermodynamically stabilizes the austenite, hence enabling martensite-to-austenite reversion upon modest annealing [32,33]. This effect can be used to tune the TRIP effect during the following mechanical test [26–30,34–36]. Al is added to form nanoprecipitates together with Ni and Mn inside the martensite matrix phase, creating the maraging effect [37,38]. We reduced the C content (~0.01 mass%) in order to ensure good weldability and better ductility of the as-quenched martensite [39].

The steel ingot was cast in a vacuum induction furnace and hot rolled at 1100 °C. After homogenization at 1100 °C for 1 h and quenching to room temperature, reversion of α′ martensite to austenite was achieved by further annealing at 450 °C or 600 °C for various periods (1 h, 4 h or 8 h) and subsequent quenching in water [25,37,40]. Here we focus on results from as-quenched and 600 °C 1 h and 8 h aged samples (from hereon referred to as S_{aq}, S_{1h}, S_{8h}), which allow us to study the micromechanical details associated with the interaction of dislocation slip, deformation-induced phase transformation and twinning during deformation.

To investigate the influence of reverted austenite (γ_{RN}) on the mechanical properties under both quasistatic and dynamic loading conditions two kinds of mechanical tests were performed. Uniaxial tensile tests were carried out at room temperature with an initial strain rate of 10^{-3} s^{-1}. Impact tests covered a temperature range of −150 °C to 100 °C. For the tensile tests, a Kammrath and Weiss stage was used, and the strain was measured by digital image correlation (DIC) using Aramis software (GOM GmbH). The impact test was carried out on subsize Charpy V-notched samples with a ligament size of 3×4 mm^2 machined along the rolling direction according to the standard DIN 50 115. The active deformation mechanisms in the microstructure were investigated by post mortem microstructure characterization of the fractured tensile samples at known strain levels determined by DIC. For these analyses scanning electron microscopy (SEM) based electron backscatter diffraction (EBSD), electron channeling contrast imaging (ECCI) and secondary electron (SE) imaging methods, as well as transmission electron microscopy (TEM) and synchrotron X-ray diffraction (SXRD) analyses were employed. Moreover, in situ SEM tensile and three-point bending tests were performed. The former focused on the analysis of γ_{RN} stability and microcrack-arresting mechanisms. The latter provided insight on strain partitioning between the martensite and γ_{RN} grains.

For the SEM analysis JEOL JSM-6500F (for EBSD, SE), Zeiss-Crossbeam XB 1540 FIB-SEM (for in situ ECCI and in situ EBSD) and Zeiss-Merlin (for post mortem ECCI) instruments were used. EBSD measurements were carried out under an acceleration voltage of 15 kV with a step size of 80 nm. TEM observations were performed in a JEOL JEM-2200FS operated at 200 kV. Specimens for TEM analysis were prepared from 3 mm disks of tensile samples. The sample preparation methodology for SEM and TEM analyses are explained elsewhere [41].

Synchrotron measurements were performed at the high resolution powder diffraction beamline P02.1 at PETRA III (DESY Hamburg, Germany), using synchrotron radiation at a wavelength of $\lambda = 0.20727$ Å. An incident beam with dimension of 200×200 μm^2 was used. After penetrating through a 1 mm thick sample with known pre-strain values, the two-dimensional XRD patterns were collected using a fast image plate detector Perkin Elmer 1621 (2048×2048 pixels, 200×200 μm^2 pixel size, intensity resolution of 16 bit), which was placed at a distance of 800 mm to the sample. XRD patterns were integrated into the 2θ space using the software FIT2D [42].

3. Results

3.1. Influence of aging on the microstructure

The partial transformation of α′ martensite back to γ_{RN} during annealing at 600 °C is shown in Fig. 1 for the as-quenched sample (S_{aq}), the 1 h heat-treated sample (S_{1h}) and the 8 h heat-treated sample (S_{8h}) as imaged by SE imaging, EBSD phase and inverse pole figure (IPF) maps. In the quenched state, the microstructure is composed fully of α′ martensite, as shown by SE imaging of the etched sample surface (Fig. 1a_1) and the EBSD phase map (Fig. 1a_2). No retained austenite is observed within the resolution limit of the high resolution EBSD measurements carried out at a step size of 80 nm (Fig. 1a_2). The EBSD IPF map reveals that the α′ martensite laths within one block share nearly the same crystallographic orientation (within 1°) (Fig. 1a_3).

After annealing at 600 °C for 1 h, a new phase with thin layered morphology is formed inside the α′ martensite matrix (Fig. 1b_1) and it is indexed as austenite (γ_{RN}) by EBSD (Fig. 1b_2). All the γ_{RN} grains inside one α′ martensite block again have similar crystallographic orientations (within 1°) (Fig. 1b_3).

With increasing the annealing time to 8 h, γ_{RN} grains further grow into the α′ martensite (Fig. 1c_1–c_3), resulting in the formation of a duplex nanolayered α′ martensite–austenite microstructure. In addition, a small amount of ε martensite, i.e. less than 4 vol.%, is also present in the microstructure after the reversion treatment.

The α′ martensite and γ_{RN} phases in the S_{8h} specimen (600 °C, 8 h) are revealed in terms of a low magnification EBSD phase map, and further characterized by TEM in Fig. 2. The STEM image (Fig. 2b) provides a higher resolution image of the duplex structure with γ_{RN} grains finely distributed in the α′ martensite matrix. Details of the α′ martensite and γ_{RN} are revealed by high magnification images in Fig. 2c and d, as guided by the red and green rectangles, respectively. The α′ martensite matrix contains nanoprecipitates and a high density of dislocations (Fig. 2c). The γ_{RN} grains, in contrast, are free of

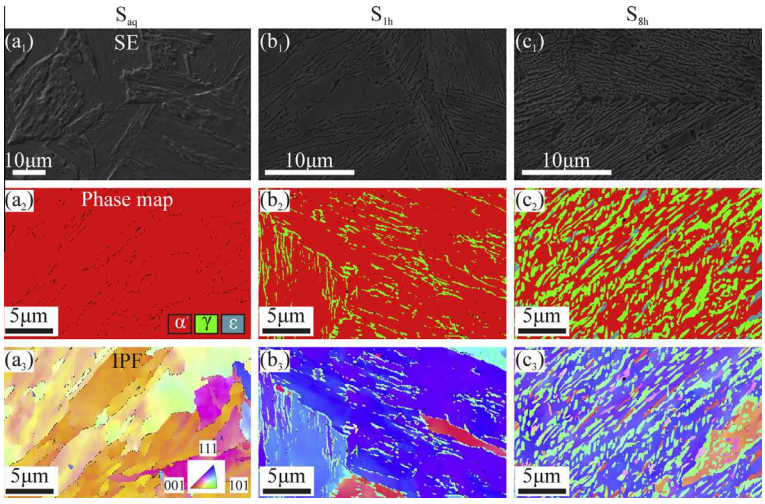

Fig. 1. Aging-induced microstructure evolution from (a) S_{aq} to (b) S_{1h} to (c) S_{8h} shown by SE imaging (1), EBSD phase map (2) and inverse pole figure (IPF) map (3). S_{aq}: as-quenched sample; S_{1h}: 1 h heat-treated sample; S_{8h}: the 8 h heat-treated sample.

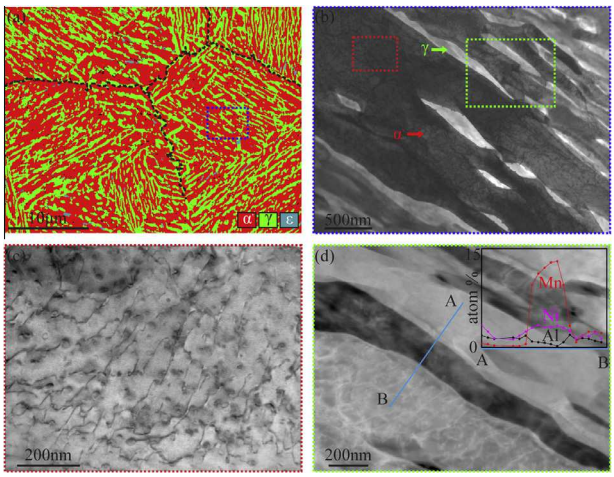

Fig. 2. Microstructure characterization of S_{8h}: (a) EBSD phase map; (b) STEM bright field image; (c) high magnification micrograph showing nanoprecipitates and high density dislocations in α′ martensite; and (d) high magnification micrograph of the γ_{RN}. The three rectangles only serve to indicate the scale transition, and do not represent the exact area from which the higher magnification image has been obtained. Prior austenite grain boundaries are indicated by black dashed line in (a). Chemical composition of α′ martensite matrix and γ_{RN} grain along the blue line A–B are shown as inset in (d). S_{8h}: the 8 h heat-treated sample.

precipitates and dislocations. The chemical compositions of α′ martensite matrix and γ_{RN} grain are shown as the inset in Fig. 2d in terms of an EDX analysis conducted in the TEM. Compared to the initially uniform distributions of all elements in the as-quenched state (sample S_{aq}), the reversion process leads to partitioning of Mn and Ni into the γ_{RN} grains, as well as of Al and Fe into the α′ martensite matrix in the 8 h annealed sample S_{8h}. Further details of this partitioning is shown in Ref. [41].

3.2. Influence of aging on the mechanical properties

The influence of γ_{RN} on the mechanical properties is examined for samples S_{aq}, S_{1h} and S_{8h} by uniaxial tensile tests at room temperature and impact tests over a temperature range from −150 °C to 100 °C (Fig. 3). The engineering stress–strain curves are presented in Fig. 3a. It is clear that the formation of γ_{RN} in α′ martensite via a reversion treatment at 600 °C leads to a pronounced increase in uniform elongation, namely, from 2.4% for the as-quenched state (sample S_{aq}) to 9.9% after 1 h annealing at 600 °C (sample S_{1h}) to 17.1% after 8 h annealing at 600 °C (sample S_{8h}). This improved ductility is not achieved at the expense of strength, i.e., the ultimate tensile strength (UTS) decreases from 925 MPa only to 920 MPa to 900 MPa. This corresponds to less than 0.6% decrease from sample S_{aq} to sample S_{1h}, and less than 2.8% decrease from sample S_{aq} to sample S_{8h}.

The DIC-based strain profiles along the gauge length of three representative tensile test samples are presented in Fig. 3b. These plots represent two deformation stages: (i) onset of strain localization (dashed lines); (ii) last stage prior to sample fracture (solid lines). The comparison of the strain profiles of the three materials at the onset of strain localization reveal that the introduction of γ_{RN} into α′ martensite leads to a delay of strain localization. The comparison of the strain profiles prior to fracture reveals the build-up of local strain during the post-necking deformation process. Apparently, in addition to the increase in uniform elongation, the presence of γ_{RN} also causes an increase in post-necking elongation, e.g. ~30% from sample S_{aq} to sample S_{1h}, and 41% from sample S_{aq} to sample S_{8h}.

Besides quasistatic uniaxial tensile tests, the three materials were also tested under dynamic loading conditions, i.e. by impact tests (Fig. 3c). Compared to S_{aq}, both reversion-annealed samples S_{1h} and S_{8h} show improved toughness properties, as seen by the increase of the upper shelf energy value at the high temperature range and the decrease in the ductile-to-brittle transition temperature (DBTT) to the lower temperature range (i.e. from 9 °C to −49 °C to −76 °C, respectively). Here DBTT is defined as the temperature at which half of the upper shelf energy is reached in the impact test.

All mechanical properties of the three sample states are summarized in Fig. 3d. It can be seen that through the introduction of the γ_{RN} reversion phase into the α′ martensite matrix, a consistent improvement in both ductility and

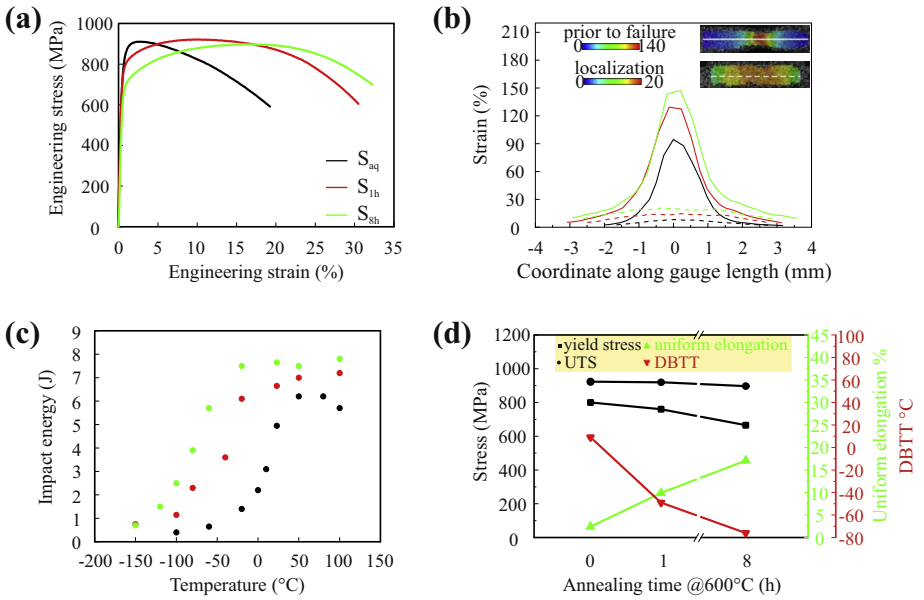

Fig. 3. For S_{aq}, S_{1h} and S_{8h}: (a) the mechanical behavior under uniaxial tensile loading; (b) the DIC strain profiles along the gauge lengths of tensile samples at onset of necking (dashed line) and the last stage prior to failure (solid line); (c) the toughness properties obtained by impact tests carried out between −150 °C and 100 °C. Yield stress is defined as $\sigma_{0.2}$. DBTT is ductile-to-brittle transition temperature. The trends in the mechanical properties obtained from these experiments are summarized in (d). S_{aq}: as-quenched sample; S_{1h}: 1 h heat-treated sample; S_{8h}: the 8 h heat-treated sample.

toughness is achieved, with only limited sacrifice of yield or UTS.

The true stress–strain curves, the strain-hardening rate curves and the evolution of the γ_{RN} fraction during uniaxial tensile testing are shown in Fig. 4. The γ_{RN} fraction is obtained from large field of view EBSD measurements [41]. When comparing the as-quenched sample S_{aq} with the heat-treated samples, S_{8h} with its highest initial γ_{RN} fraction exhibits a higher overall strain-hardening rate throughout the deformation process. The γ_{RN} fraction decreases continuously during uniform deformation (Fig. 4).

The improvements are most clearly observed for the 8 h heat-treated sample, S_{8h}. Thus, in the following sections, to provide an in-depth understanding of the underlying micromechanisms responsible for the improvements in mechanical properties, a detailed analysis of deformation mechanisms is presented for this material. Based on the strain-hardening regime shown in Fig. 4, the deformation process of the 8 h reversion treated sample S_{8h} can be divided into three stages: (i) early uniform deformation regime between 0 and 0.05 strain; (ii) late uniform deformation between 0.05 and 0.15 strain; and (iii) strain localization and failure between 0.15 and 0.20 strain.

Given the differences in the constitution of the two phases, a variety of deformation mechanisms, e.g. slip of partial dislocations, mechanical twinning, martensitic phase transformation in γ_{RN} and slip in the α' martensite matrix, are expected to be active, leading to strong strain and stress partitioning. Thus, the focus in the analysis will be placed on strain partitioning processes between the γ_{RN} and the α' martensite phases during the first two stages (i) and (ii); and on damage and failure mechanisms, occurring predominantly during stage (iii).

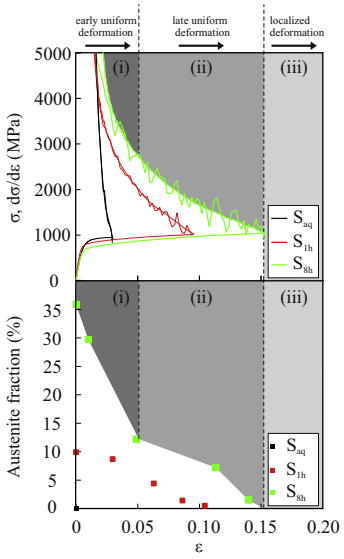

Fig. 4. The true stress–strain curve, the strain-hardening ($d\sigma/d\varepsilon$) curve and the evolution of γ_{RN} fraction during uniaxial tensile tests for S_{aq}, S_{1h} and S_{8h}. Three different deformation regimes are highlighted for S_{8h}. S_{aq}: as-quenched sample; S_{1h}: 1 h heat-treated sample; S_{8h}: 8 h heat-treated sample.

3.3. Deformation micromechanisms

The strain partitioning between the γ_{RN} and α' martensite is examined by employing a multiprobe approach using in situ SEM three-point bending tests (Fig. 5a–c), in situ SEM tensile tests with EBSD (Figs. 5d and e and 9), post mortem TEM (Fig. 6b_1 and b_2), SXRD (Fig. 6c) and SEM (Figs. 6a_1–a_4, 7 and 8) based observations.

We start the analyses with in situ bending, which reveals the microstructural heterogeneity of the deformation

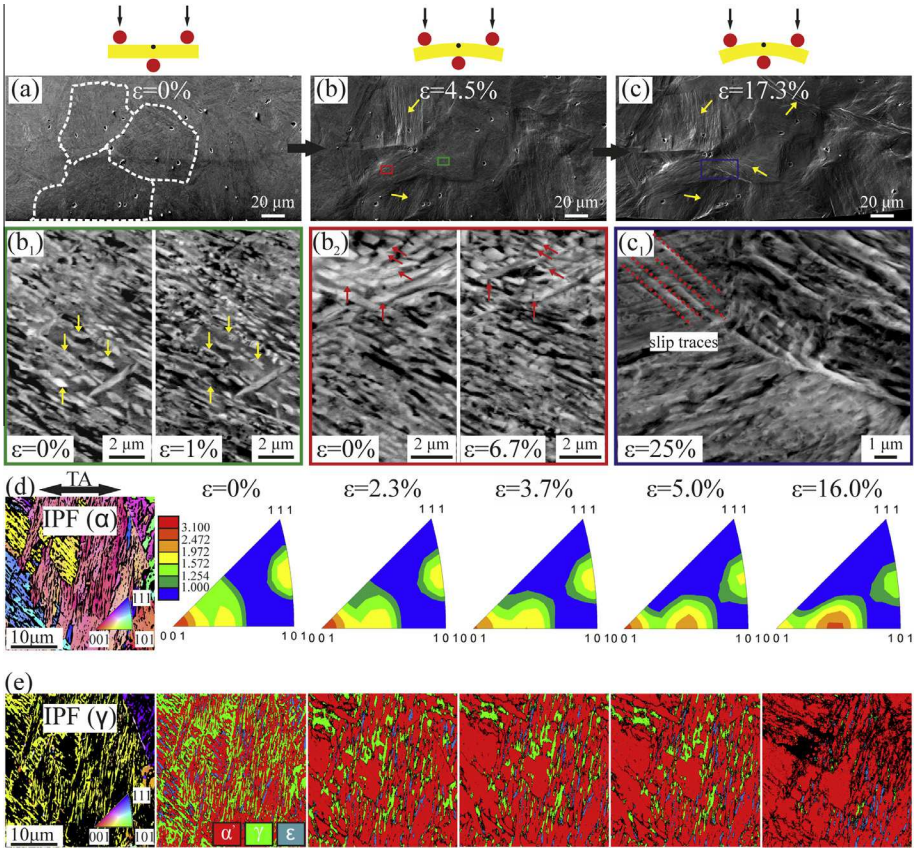

Fig. 5. Evolution of surface topography of S_{8h} on the tension side during in situ three-point bending test in high resolution SEM: (a) undeformed state; (b) after 4.5% local deformation; (c) after 17.2% local deformation. The white dashed lines in (a) illustrate the prior γ grain boundaries. Three zoom-in BSE images show local microstructure at different levels of local strain. EBSD maps obtained during in situ SEM tensile test of S_{8h}, revealing (d) IPF map of α′ martensite prior to deformation, and the evolution of crystallographic orientation during deformation; (e) IPF map of γ_{RN} prior to deformation, and evolution of phase maps with straining. S_{8h}: 8 h heat-treated sample. (For interpretation of the references to colour in this figure legend, the reader is referred to the web version of this article.)

behavior (Fig. 5a–c). In order to correlate it to the strain partitioning process during uniaxial tensile testing, the region under tensile load of the three-point bending sample was examined by SE and BSE imaging. After the first bending step (corresponding to ~4.5% local tensile strain), the polished flat surface (Fig. 5a) roughens to different levels in different regions (Fig. 5b) corresponding to different prior γ grains (see white dashed outlines that indicate typical prior γ grain size in Fig. 5a). At this strain level, slip steps are only observed in a few regions (see, e.g., yellow arrows in Fig. 5b). Since the α′ martensite can accommodate plasticity only via dislocation slip, the absence of slip steps indicate that the α′ martensite is plastically deformed only in these few preferred regions. Mine et al. [13] also showed that plastic deformation in the α′ martensite is preferentially activated in regions with favored orientations, e.g. with highest Schmid factors with respect to the external loading. Apparently, at this early uniform deformation regime the α′ martensite matrix accommodates only a limited portion of the applied strain. However, the overall strain level (~4.5%) clearly indicates that the microstructure is in the plastic deformation regime (Fig. 5b). To reveal how plastic deformation proceeds within those regions where no pronounced slip lines are observed, high-magnification before–after BSE images are shown in Fig 5b_1 and b_2. These images reveal two distinct processes. On the one hand, in some smaller γ_{RN} grains gradual contrast changes are observed such that a fraction of the γ_{RN} grains loses contrast with the surrounding martensite, as indicated by yellow arrows in Fig. 5b_1. These, as will be discussed next with the HR-EBSD data in Fig. 5e, correspond to the TRIP effect. On the other hand, mechanical nanotwins are formed within some relatively large γ_{RN} grains, as indicated by red arrows in Fig 5b_2. TEM based confirmation of the mechanical twinning, and the size-dependent competition between transformation and mechanical twinning, can be found elsewhere [41]. Both of these mechanisms are triggered in the early uniform deformation regime (i) and are active until the end of the late uniform deformation regime (ii), as was already shown for the TRIP effect in Fig. 4b. Depending on their crystallographic orientation, some γ_{RN} grains are transforming at lower strains than others [41]. At the later stages of bending (~17.3% tensile strain), slip steps are observed in most regions (see additional yellow arrows in Fig. 5c). As highlighted by the red dashed lines in the high magnification BSE image presented in Fig. 5c_1, these slip traces now also penetrate through (transformed) γ_{RN} regions. This implies a larger contribution of martensite plasticity during this later stage of deformation. Further insight into the evolution of strain

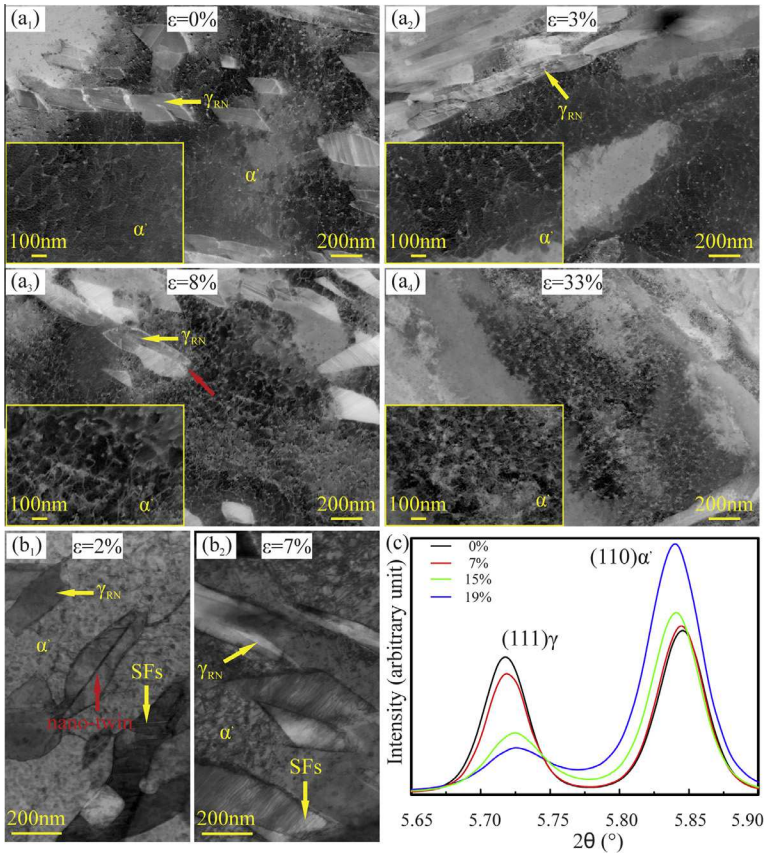

Fig. 6. Microstructure overview for S_{8h} by post mortem ECCI analysis at different strain levels: (a_1) undeformed; (a_2) 3%; (a_3) 8%; (a_4) 33%; and STEM analysis at (b_1) 2%; (b_2) 7%; and (c) synchrotron X-ray diffraction profiles for (1 1 1) γ_{RN} and (110) α' martensite peaks. S_{8h}: 8 h heat-treated sample. (For interpretation of the references to colour in this figure legend, the reader is referred to the web version of this article.)

partitioning between α' martensite and γ_{RN} during deformation is provided from in situ HR-EBSD measurements conducted during tensile tests (Fig. 5d and e).

Here, the evolution of the α' martensite texture and of the γ_{RN} phase fraction are shown for the 8 h reversion annealed specimen S_{8h}. The crystallographic orientation of the α' martensite matrix and of the γ_{RN} phase prior to deformation are shown with respect to the tensile axis (TA) on the left-hand side of Fig. 5d and e, respectively[1]. As shown in Fig. 5d, no significant change in α' martensite grain orientation takes place up to 3.7% strain. During further deformation to 16.0% strain, a clear difference emerges in the IPF maps. Two mechanisms can be responsible for the texture changes in the α' martensite matrix: (i) crystal rotation due to dislocation slip-mediated plasticity; (ii) deformation-induced martensite. In the current sample the γ_{RN} phase and α' martensite phase share a Kurdyumov–Sachs orientation relationship prior to deformation (not shown here). Thus, when the γ_{RN} phase transforms to α' martensite during loading, the deformation-induced martensite exhibits only minor misorientation with respect to the surrounding tempered α' martensite (within ~1°). Therefore, the observed crystal rotation is attributed to dislocation slip in the α' martensite matrix. The fact that this rotation takes place above 3.7% global strain reveals that dislocation plasticity in α' martensite mainly takes place in the later uniform deformation regime (ii).

From the phase maps we observe that the γ_{RN} phase transforms into α' martensite faster at the initial loading stage, e.g. between 0% and 2.3% strain. The transformation slows down towards the later uniform deformation regime, e.g. between 2.3% and 5.0% strain (and later up to 16% strain). A similar trend of the γ_{RN} transformation rate and behavior is observed from the ex situ EBSD measurements from the bulk of deformed samples shown in Ref. [41], ruling out the influence of surface effects in the results presented in Fig. 5. Thus, we confirm that, besides the mechanical twinning process observed in Fig. 5b_2, γ_{RN} accommodates strain also via deformation-induced phase transformation. The activation of both the twinning-induced plasticity (TWIP) and the TRIP mechanisms at low strain levels indicates the stronger role of the γ_{RN} grains in the overall strain accommodation process at low deformation levels.

The details of how plastic deformation and phase transformation proceed in the α' martensite and γ_{RN} grains are shown by post mortem ECCI (Fig. 6a_1–a_4) and TEM analyses (Fig. 6b_1 and b_2). Prior to deformation, α' martensite contains nanoparticles and dislocations, as shown by the ECCI image and high magnification image as inset in Fig. 6a_1. No significant multiplication of dislocations in α' martensite is observed after further straining to 3% strain (Fig. 6a_2), confirming that α' martensite does not

[1] Due to the difficulty of distinguishing between tempered α' martensite and deformation-induced martensite by EBSD measurements, we treat all α' martensite in the microstructure as α' martensite matrix.

enter the plasticity regime yet. However, a pronounced increase in dislocation density and interaction between dislocations and nanoparticles are observed after 8% strain (Fig. 6a$_3$), indicating plastic deformation of α′ martensite at this stage of deformation. Massive multiplication of dislocations takes place during further straining, e.g. after 33% strain shown in Fig. 6a$_4$. γ_{RN} grains, on the other hand, accommodate strain from the beginning of deformation, as observed by the continuous increase of stacking faults and twin boundaries (see red arrows in Fig. 6) from Fig. 6a$_1$ to Fig. 6a$_3$. The ECCI observations are also validated by the TEM analysis shown in Fig. 6b$_1$ and b$_2$.

Further confirmation of the strain partitioning between γ_{RN} and α′ martensite is provided by the post mortem synchrotron X-ray diffraction measurements. Tensile fractured samples with known local strain values from DIC were analyzed by synchrotron X-ray diffraction, as shown in Fig. 6c. Here, diffraction profiles for (1 1 1) γ_{RN} and (1 1 0) α′ martensite peaks for the sample globally strained to different values are shown. Since diffraction peaks of deformation-induced martensite overlap with those of tempered α′ martensite, all α′ martensite present in the microstructure is treated as α′ martensite matrix. As shown in Fig. 6c, the intensity of the (1 1 1) γ_{RN} peak gradually decreases with deformation while that of the (1 1 0) α′ martensite peak continuously increases, indicating the occurrence of deformation-induced martensitic transformation. This transformation behavior is consistent with previous HR-EBSD measurements (Figs. 4 and 5e). At the same time, the peak profile of (1 1 1) γ_{RN} exhibits an asymmetric broadening and shifting to higher 2θ values. However, the (1 1 0) α′ martensite peak is symmetrically broadening, especially after 7% macroscopic strain and shifting to lower 2θ values with ongoing deformation. An asymmetric broadening and shifting to higher 2θ values of the austenite peaks implies the formation of stacking faults and twins [43]. Symmetric broadening and shifting to lower 2θ values in martensite indicates multiplication of dislocations with increasing deformation [44].

All these analyses carried out by in situ three-point bending measurements (Fig. 5a–c), ECCI (Fig. 6a$_1$–a$_4$) and TEM analysis (Fig. 6b$_1$ and b$_2$), synchrotron X-ray diffraction measurements (Fig. 6c), in situ EBSD (Fig. 5d and e) and ex situ EBSD measurements (Fig. 4) suggest the following structure evolution sequence. At early stages of deformation, γ_{RN} accommodates the majority of the plastic strain by the formation of stacking faults, mechanical twins and succeeding phase transformation. Apart from a few favorably oriented martensite regions, the majority of the martensitic matrix enters into the plastic regime during the late uniform deformation stage. Thus, in this second regime, plasticity is accommodated both by the γ_{RN} and martensite, while the (high defect density) freshly transformed martensite regions (previous γ_{RN} grains) do not show indications of plasticity. Only at very high deformation levels within the localized neck is limited further plastic deformation of the freshly transformed martensite observed.

3.4. Damage and failure micromechanisms

The third regime defined in the hardening curve (Fig. 4) is probed next by analyzing the damage evolution (i.e. microcrack nucleation and growth) process during deformation. The damage micromechanisms are examined by post mortem SEM analysis on tensile fractured samples on the basis of well-defined local strain values obtained from the DIC-based measurements (Figs. 7 and 8) and in situ SEM analysis (Fig. 9).

We begin our analyses by comparing the damage evolution process and the fracture surface topography of the as-quenched sample S_{aq} and the 8 h reversion heat-treated material S_{8h}, as shown in Fig. 7a$_1$–a$_4$, Fig. 7b$_1$–b$_4$, respectively. In both materials, up to necking we observe only a limited amount of damage incidents. After necking of sample S_{aq}, microcracks of several μm are nucleated, as shown by the high magnification inset in Fig. 7a$_1$. These incidents are heterogeneously distributed in the microstructure. With further straining towards fracture, the number of damage

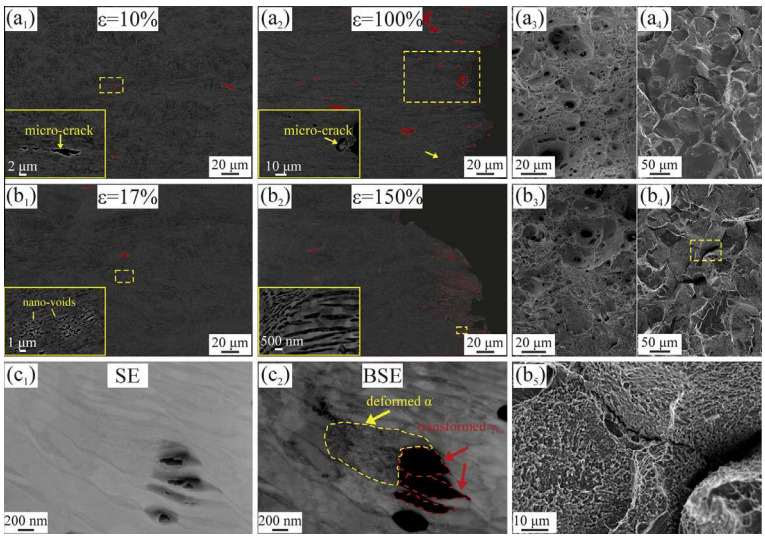

Fig. 7. Damage evolution process for S_{aq}: (a$_1$) BSE image of necking area; (a$_2$) BSE image of area close to fracture surface; (a$_3$) fracture surface of sample tensile tested at room temperature; (a$_4$) fracture surface of sample impact tested at −196 °C. For S_{8h}: (b$_1$) BSE image of necking area; (b$_2$) BSE image of area close to fracture surface; (b$_3$) fracture surface of sample tensile tested at room temperature; (b$_4$) fracture surface of sample impact tested at impact test at −196 °C and (b$_5$) high magnification image of the fracture surface in b$_4$. High magnification BSE images are shown as inset for corresponding images. (c$_1$, c$_2$) High resolution SE and BSE images of microcracks in S_{8h}. S_{aq}: as-quenched sample; S_{8h}: 8 h heat-treated sample.

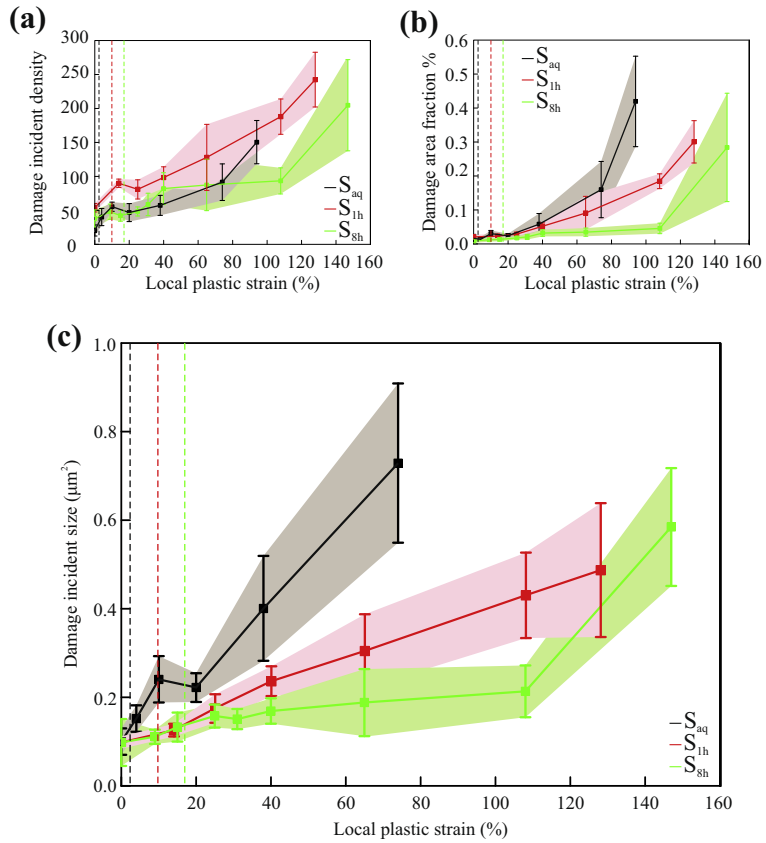

Fig. 8. Quantification of damage mechanisms in S_{aq}, S_{1h} and S_{8h} as a function of deformation: (a) damage incident density; (b) damage area fraction; (c) damage incident size. Dash line indicates the necking strain for each sample. S_{aq}: as-quenched sample; S_{1h}: 1 h heat-treated sample; S_{8h}: 8 h heat-treated sample.

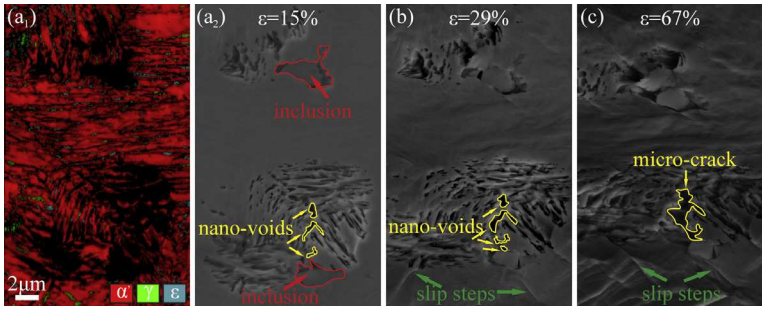

Fig. 9. Interactions of microcracks with the surrounding phases in S_{8h} revealed by in situ tensile test (a_1) EBSD phase map; (a_2) SE imaging of area in a_1; (b, c) SE imaging of this area after further straining to 29% and 67%, respectively. S_{8h}: the 8 h heat-treated sample. (For interpretation of the references to colour in this figure legend, the reader is referred to the web version of this article.)

incidents increases, as well as the size of the cracks (see inset in Fig. 7a_2). Sample S_{aq} exhibits a ductile failure behavior at room temperature, with a dimpled fracture surface (Fig. 7a_3). However the impact test sample fractured at −196 °C shows a cleavage-type fracture surface (Fig. 7a_4), which is in accordance with the low impact energy shown in Fig. 3.

A more unexpected damage evolution process is observed in the austenite reversion sample S_{8h}. After necking, numerous nanovoids are nucleated in the microstructure, as shown by the high magnification inset in Fig. 7b_1. In contrast to the formation of microcracks observed in the S_{aq} material, these nanovoids in sample S_{8h} remain confined by the nanolaminated microstructure morphology. The tips of the majority of the nanovoids are round, indicating significant plastic deformation at the crack tip. Further deformation to fracture leads to massive nucleation of such nanovoids. Interestingly, in many cases formation of larger cracks by coalescence of these nanovoids is delayed, even when the void spacing is decreased to values below ~100 nm. Higher magnification SE and BSE images shown in Fig. 7c_1 and c_2 reveal that the nanocracks are initially nucleated at the boundary between deformed martensite regions (with high dislocation density) and the freshly transformed martensite (see Fig. 7c_1). Further deformation leads to the full delamination of the individual grains at the

interface (see the shallow cavity in the SE image in Fig. 7c_1 with respect to the surrounding flat cross-section). However, these cracks are successfully arrested due to the nanolaminated microstructure present (see Fig. 7b_2 for an overview and Fig. 7c_2 for a high magnification view of an interface crack stopped at the neighboring deformed α′ martensite shown with the yellow arrow). Consequently, the specimen S_{8h} exhibits ductile failure behavior at room temperature with a fracture surface consisting of dimples (Fig. 7b_3). Similar to the case of the S_{aq} material there is a transition to brittle behavior upon impact testing at –196 °C. However, in contrast to S_{aq}, the fracture demonstrates fibrous surface features, a footprint of the plastic deformation of the nanoscale duplex martensite-reverted austenite microstructure (Fig. 7b_4 and magnification image in Fig. 7b_5).

To further understand the influence of the microstructure on the deformation-induced damage evolution shown in Fig. 7, the damage evolution process is quantified in Fig. 8. For different DIC-based local plastic strain levels, SE images with optimized crack contrast are obtained by high resolution SEM. These images are analyzed using the Image J software [45,46] to determine the evolution of the damage incident density (Fig. 8a) and the damage area fraction (Fig. 8b) as a function of the local plastic strain. The average damage incident size corresponding to different stages of deformation is calculated using the two data sets and plotted in Fig. 8c.

Within the uniform deformation regime, all samples contain only a small area fraction of microcracks (~0.01%). After necking, as indicated by dashed lines in Fig. 8a, the damage incident density shows an almost monotonous increase with local plastic strain for both samples S_{aq} and S_{1h}. For sample S_{8h}, however, this increase proceeds at a slower rate up to very high strain levels (~150%). A similar evolution with local plastic strain exists for the damage area fraction of all samples, where a drastic early increase is present for sample S_{aq} and a moderate and respectively slow increase for samples S_{1h} and S_{8h} (Fig. 8b). Thus, compared to S_{aq} and S_{1h}, the 8 h reversion treated specimen S_{8h} always shows the smallest crack size during deformation (Fig. 8c), revealing the effect of damage arresting mechanisms. To reveal this mechanism in more detail, we examine how deformation further proceeds in the S_{8h} microstructure when cracks are nucleated. For this purpose, a S_{8h} sample is pre-strained to 15% strain, then re-polished and further deformed in situ in the SEM (Fig. 9). The EBSD phase map and SE image of the first state are shown in Fig. 9a_1 and a_2. The latter shows the presence of two inclusions (outlined by red in Fig. 9a_2). Due to incompatible deformation with microstructure and resulting stress concentration in the neighborhood, inclusions inevitably act as damage sites. What is important here to underline is that even when inclusions are present, the nucleated damage is successfully arrested through nanovoid coalescence (outlined by yellow in Fig. 9b and c), enabling the further strain accommodation of the surrounding α′ martensite matrix by the formation of slip steps (as indicated by green arrows in Fig. 9c).

4. Discussion

4.1. Overview of deformation micromechanisms

A schematic sketch of the deformation, damage and failure micromechanisms in the 8 h reversion heat-treated sample S_{8h} is shown in Fig. 10.

The microstructure of the S_{8h} material consists of the α′ martensite phase (phase in red) and the γ_{RN} phase (phase in green) prior to deformation (Fig. 10a). At small strains (Fig. 10b), the γ_{RN} phase (phase in green) partitions the majority of the strain via multiple deformation mechanisms, i.e. formation of twins (area in gray), stacking faults (area in yellow) and martensitic phase transformation (phase in red). At this early stage of deformation, only certain α′ martensitic regions with preferred (soft) orientations are plastically deformed as documented by slip traces (black lines in Fig. 10b). With progressively increasing strain (Fig. 10c), more martensitic regions become plastic and a co-strain partitioning process of both the γ_{RN} phase and the α′ martensite phase is observed. During further straining up to the late uniform deformation regime (Fig. 10d), the martensitic phase transformation is

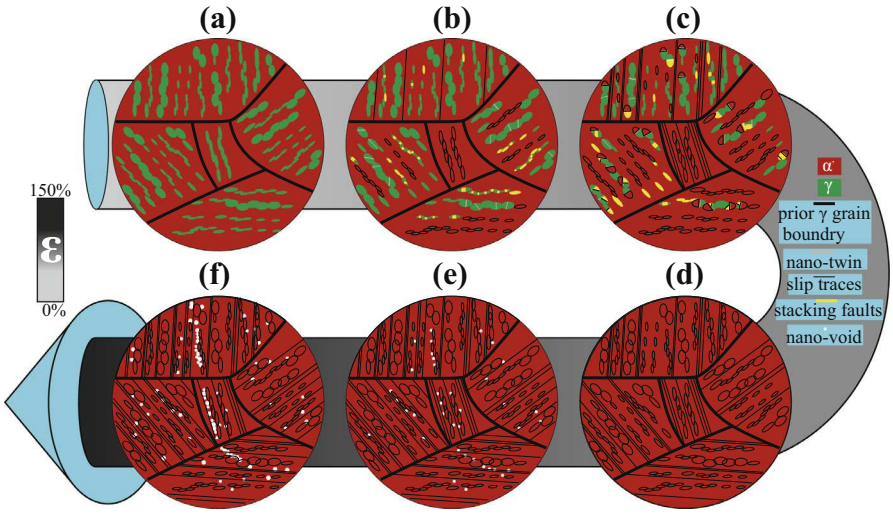

Fig. 10. Schematical sketch of the deformation, damage and failure micromechanisms in the 8 h reversion heat-treated sample S_{8h}. (For interpretation of the references to colour in this figure legend, the reader is referred to the web version of this article.)

completed and all martensitic regions are rendered plastic. However, the two types of martensite (deformed martensite vs. freshly transformed martensite) have different defect densities and compositions, but still carry the morphology of the initial reverted austenite–martensite nanolaminate microstructure. Hence, a composite-like behavior is still expected during the further deformation, even when both nanolaminate materials are indexed as "martensite". In the post-necking regime (Fig. 10e and f), the damage process is taking place via nucleation and coalescence of nanovoids, but most incidents stay confined by this inherited nanolaminate microstructure morphology. Such a sandwich effect is also reported by other works [19–22].

The analysis provided here underlines that the deformation-induced martensitic transformation and the associated defect density evolution actively modify the microstructural strain partitioning process. We refer to this phenomenon as dynamic strain partitioning.

4.2. Relationship between mechanical properties and deformation micromechanisms

As demonstrated above, aging-induced changes in the microstructure influence the overall mechanical properties profoundly, especially regarding the yield strength, the hardening behavior and the overall ductility. In the following discussion of the relationship between deformation micromechanisms and these mechanical enhancements, we place special emphasis on the analyses of the strain-hardening behavior and damage resistance, which play critical roles in the improvements achieved by the aging treatment. It should be considered, however, that the enhancements of these properties are intrinsically inter-linked with each other, and often there are multiple micromechanisms that contribute to the observed effect. For example, the yield strength is decreased by the decrease in dislocation density in the α' martensite due to annealing at 600 °C, but also by the coarsening of the nanoparticles during annealing at 600 °C and by the replacement of some of the hard α' martensite regions with the soft γ_{RN} reversion grains [47,48]. Another example is regarding the preservation of the high UTS upon the reversion treatment. Here the role of the precipitation hardening micromechanism (i.e. the maraging effect) is definitely important; however, the factors that play a role in improving the strain-hardening rate or limiting the damage-induced softening (both of which will be discussed next) also play an indirect role.

The improved strain-hardening can be explained through the presence of various deformation mechanisms and the resulting dynamic strain partitioning process. In the early uniform deformation regime (between 0 and 0.05 strain) the "softer" γ_{RN} phase dominates the deformation process through its intrinsic multiple deformation mechanisms, i.e. mechanical twinning (TWIP) (Fig. 5b_2), dislocation slip, formation of SFs (Fig. 6) and deformation-induced martensitic transformation (TRIP) (Figs. 4, 5e and 6c). However, due to the wide variation in the stability of the γ_{RN} grains (promoted by their size distribution and the resulting competition between twinning and transformation [41]), the associated phase transformation proceeds also to the late uniform deformation regime (Fig. 4). Note that such beneficial variations in austenite stability can also be introduced through variations in C content, the crystalline and phase neighborhood, as reported by Jacques et al. [49]. The α' martensite plasticity starts in the late uniform deformation regime (from 0.05 onwards) as confirmed by the formation of slip steps (Fig. 5c_1), evolution of the typical body centered cubic deformation texture [50,51] (Fig. 5d) and an increased dislocation density (Fig. 6a_1–a_4 and c). Thus, the presence of well-dispersed TRIP–TWIP behavior enables the strain-hardening capacity of the α' martensite matrix to be more conservatively consumed. The contribution of martensite strain-hardening is significant in this aged sample, as the martensite-to-austenite reversion process causes nanoprecipitation [24,37] and a dislocation density decrease in the α' martensite, leading to improved α' martensite strain-hardening during plastic deformation through dislocation multiplication and their interaction with nanoparticles, e.g. via the Orowan mechanism [52–58]. The importance of these beneficial effects is underlined upon comparison to the control sample S_{aq}, in which the strain-hardening capacity of α' martensite is quickly exhausted and early necking is observed. In summary, the presented observations here also clarify that microstructures consisting of an (initially softer) metastable phase with a wide dispersion in transformation stability, and an (initially harder) phase with further strain-hardening capacity, provide an ideal overall strain-hardening response upon deformation. Similar indications are also observed in other works in the literature, for example, studying the strain/stress partitioning behavior in several TRIP-assisted steels, Tomota et al. [59] reported the importance of optimizing the critical stress for ferrite plasticity and deformation-induced martensitic transformation, for improved mechanical properties.

Given the additional deformation reserve created by the replacement of the less ductile martensite by ductile austenite, and the well-optimized strain-hardening behavior explained above, increased uniform ductility in TRIP-maraging steels is not surprising. However, considering that almost all the γ_{RN} grains are transformed prior to plastic instability (Fig. 4), the increased post-necking ductility is unexpected. We attribute this improvement to the crack-arresting ability of the microstructure, which is in turn provided by its nanolaminate morphology. In the reversion-free material S_{aq}, continuous nucleation and monotonic growth of microcracks are observed with increasing strain after the onset of strain localization (Fig. 7a_1–a_4). In low carbon martensitic steels, martensite laths within one block are characterized by low angle misorientations [60]. This means that once a crack is initiated in such a microstructure, it can propagate along the {0 0 1} planes through the microstructure without experiencing large obstacles from these small angle grain boundaries [61]. In the reversion-treated material S_{8h}, on the other hand, damage is nucleated in the microstructure as interface nanovoids, which later undergo coalescence into nanocracks covering the full interface. However, the neighboring deformed martensite and fresh martensite regions (creating the nanolaminate morphology) inhibit the further growth of the damage incident with increasing strain (Fig. 7b_1–b_5 and c_1–c_2). In other words, the high interface density and the specific interface morphology promote a high crack-arresting ability to the microstructure [25]. Even in the extreme case of inclusion damage, the nucleated cracks can be successfully arrested and confined by the nanolaminate morphology of the microstructure. Consequently, the associated high localized stress can be re-dispersed, and local catastrophic failure is avoided (Fig. 9). Note that this mechanism of

stress-delocalization also enables the surrounding microstructure to be further deformed, enabling larger fractions of the microstructure to contribute to the strain-hardening.

The observed consistent improvements in toughness can also be regarded in connection to the enhanced crack-arresting ability of this microstructure. As reported in the literature, the influence of metastable austenite on toughness depends on the balance between the energy that is dissipated at the tip of the crack during deformation-induced martensitic transformation and the fracture properties of the transformation product [62–64]. In this regard, a propagating crack in the current TRIP-maraging steel faces the nanolaminate morphology with a high density of interface boundaries in the microstructure ahead, and the transformation-induced martensite is tougher compared to those in other TRIP steels with higher carbon contents.

4.3. Reflections on microstructure design

In TRIP-maraging steels and other TRIP-assisted steels (e.g. quenching and partitioning and/or tempering steels (Q-P-T steels)), the majority of the research efforts has so far focused on the overall influence of the austenite volume fraction and its stability on the material's strength and ductility [26–30,65–68]. Only in a few works have the underlying deformation mechanism inside each phase [69,70] or the interactions between the neighboring phases been addressed [71,72]. The results presented here on deformation, damage and failure micromechanisms in TRIP-maraging steels demonstrate the importance of these interactions, and enable a more general discussion of the targeted microstructure design. The gained understanding is more transparent upon comparison to traditional alloys and the deformation micromechanisms therein. In dual phase (DP) steels with soft ferrite matrix and hard martensite islands [17,73–76], for example, the former phase partitions the strain and the latter phase partitions the stress from the beginning of deformation onwards [76]. The mechanical properties of the constitutive phases, their respective chemical composition, the martensite volume fraction, their size, morphology and distribution have been observed to influence the strain/stress partitioning process and play an important role in the failure mechanisms [74–77]. Yet in almost all DP microstructure variants (except for TRIP-assisted UFG-DP [34,78,79]) it is effectively a static strain partitioning process (at least up to the point of localization), and only a certain portion of the entire strain-hardening capacity is consumed. In conventional TRIP-assisted multiphase steels, on the other hand, a dynamic strain partitioning process does exist due to retained austenite in the microstructure [59]. However, as a result of large grain size of the ferrite matrix crystals (above several μm), a heterogeneous partitioning of strain within the ferrite matrix grains prevails the co-deformation process, e.g. some regions in the ferrite grains do not contribute to strain partitioning at all [49]. TRIP-maraging steels, in contrast, benefit from both of these effects as the TRIP effect is introduced in a nanolaminate microstructure. This combination of transformation plasticity and size-confinement enables a larger portion of the strain-hardening capacity of the material to be exploited upon deformation. This is in accordance with other works on nanolaminated steel microstructures, giving rise to extraordinary properties, such as nanostructured bainitic steels [80,81] or pearlite [82,83].

5. Conclusions

In this work, we studied the influences of aging on the mechanical properties and the underlying deformation, damage and failure micromechanisms in a Fe–9Mn–3Ni–1.4Al–0.01C (mass%) TRIP-maraging steel. The main conclusions are as follows:

(1) As a result of aging at 600 °C both reverted nanoscale austenite films (γ_{RN}) and nanoparticles are formed inside the α' martensite, modifying the single phase α' martensite microstructure (here represented by the as-quenched material state S_{aq}) into a nanolaminate γ_{RN}-α' martensite microstructure (represented by the reversion heat-treated sample states S_{1h} and S_{8h}).

(2) From as-quenched sample S_{aq}, to 1 h heat-treated sample S_{1h}, and further to 8 h heat-treated material S_{8h}, the martensite-to-austenite reversion heat treatment leads to a continuous increase in uniform elongation (from 2.4% for S_{aq}, to 9.9% for S_{1h}, to 17.1% for S_{8h}), post-necking elongation (30% increase from S_{aq} to S_{1h}, 41% increase from S_{aq} to S_{8h}) and toughness (DBTT decreases from 9 °C for S_{aq}, to −49 °C for S_{1h}, to −76 °C for S_{8h}), with only limited sacrifice in yield strength ($\sigma_{0.2}$ decreases from 800 MPa for S_{aq}, to 760 MPa for S_{1h}, to 665 MPa for S_{8h}) and UTS (from 925 MPa for S_{aq}, to 920 MPa for S_{1h}, to 900 MPa for S_{8h}).

(3) These improvements in mechanical properties are associated with the high mechanical stability introduced by the TRIP–TWIP-induced dynamic strain partitioning and nanolaminate morphology enabled damage resistance.

(4) The dynamic nature of strain partitioning is revealed upon studying the deformation micromechanisms in the nanolaminate microstructure at different stages of deformation. In the early uniform deformation regime of the 8 h heat-treated sample S_{8h} (0–0.05 strain), the γ_{RN} phase partitions the majority of the strain via multiple deformation mechanisms, i.e. formation of twins, stacking faults and martensitic phase transformation. At these small strains (0–0.05 strain) only certain α' martensitic regions with preferred orientations are plastically deformed. At late uniform deformation regime (0.05–0.15 strain), more martensitic regions become plastic and a co-strain partitioning process of both the γ_{RN} phase and the α' martensite phase is observed.

(5) A very high damage resistance ability is obtained in the 8 h heat-treated sample S_{8h} due to the nanolaminate morphology of the microstructure. The damage process is taking place via continuous nucleation and coalescence of nanovoids, but most incidents stay confined by this inherited nanolaminate microstructure morphology.

(6) From these observations we learn that advanced steel design should provide microstructures which are capable of exploiting dynamic strain partitioning effects among constitute phases by introducing at least one unstable phase (e.g. austenite) with dispersed transformation behavior and enhanced damage resistance through nanolaminate structure.

Acknowledgements

The authors gratefully acknowledge the funding by the European Research Council under the EU's 7th Framework Programme (FP7/2007-2013)/ERC Grant agreement 290998 "SmartMet", and contributions of Monika Nellessen, Katja Angenendt, Aleksander Kostka, Benjamin Breitbach, Michael Adamek and Herbert Faul. Parts of this research were carried out at the light source PETRA III at DESY, a member of the Helmholtz Association (HGF).

References

[1] M. Nasim, B.C. Edwards, E.A. Wilson, Mater. Sci. Eng. A 281 (2000) 56.
[2] B.C. Edwards, M. Nasim, E.A. Wilson, Scr. Metall. 12 (1978) 377.
[3] K.H. Kwon, I.-C. Yi, Y. Ha, K.-K. Um, J.-K. Choi, K. Hono, et al., Scr. Mater. 69 (2013) 420.
[4] S. Morito, H. Yoshida, T. Maki, X. Huang, Mater. Sci. Eng. A 438–440 (2006) 237.
[5] G. Krauss, Hardenability Concepts with Applications to Steel. 1978.
[6] K. Nakashima, Y. Fujimura, T. Tsuchiyama, S. Takaki, Mater. Sci. Forum 539–543 (2007) 4783.
[7] H. Yang, H. Bhadeshia, Scr. Mater. 60 (2009) 493.
[8] P.J. Brofamn, G.S. Ansell, Metall. Trans. A 14A (1983) 1929.
[9] A.J. Kaijalainen, P.P. Suikkanen, T.J. Limnell, L.P. Karjalainen, J.I. Kömi, D.A. Porter, J. Alloys. Compd. 577 (2013) S642.
[10] J. Huang, Z. Xu, Mater. Sci. Eng. A 438–440 (2006) 254.
[11] M.K. Miller, P.A. Beaven, S.S. Brenner, G.D.W. Smith, Metall. Trans. A 14 (1983) 1021.
[12] S. Nagakura, Y. Hirotsu, M. Kusunoki, T. Suzuki, Y. Nakamura, Metall. Trans. A 14 (1983) 1025.
[13] Y. Mine, K. Hirashita, H. Takashima, M. Matsuda, K. Takashima, Mater. Sci. Eng. A 560 (2013) 535.
[14] G. Miyamoto, N. Iwata, N. Takayama, T. Furuhara, Acta. Mater. 60 (2012) 1139.
[15] H. Jafarian, E. Borhani, A. Shibata, N. Tsuji, J. Alloys Compd. 577 (2013) S668.
[16] T. Chiba, G. Miyamoto, T. Furuhara, Scr. Mater. 67 (2012) 324.
[17] M. Calcagnotto, Y. Adachi, D. Ponge, D. Raabe, Acta. Mater. 59 (2011) 658.
[18] M. Kehoe, P.M. Kelly, Scr. Metall. 4 (1970) 473.
[19] S. Nambu, M. Michiuchi, Y. Ishimoto, K. Asakura, J. Inoue, T. Koseki, Scr. Mater. 60 (2009) 221.
[20] C. Jeong, T. Oya, J. Yanagimoto, J. Mater. Process. Technol. 213 (2013) 614.
[21] J. Inoue, S. Nambu, Y. Ishimoto, T. Koseki, Scr. Mater. 59 (2008) 1055.
[22] F. Carreño, J. Chao, M. Pozuelo, O.A. Ruano, Scr. Mater. 48 (2003) 1135.
[23] D. Raabe, D. Ponge, O. Dmitrieva, B. Sander, Scr. Mater. 60 (2009) 1141.
[24] O. Dmitrieva, P. Choi, S.S.A. Gerstl, D. Ponge, D. Raabe, Ultramicroscopy 111 (2011) 623.
[25] D. Raabe, S. Sandlöbes, J. Millán, D. Ponge, H. Assadi, M. Herbig, P.-P. Choi, Acta Mater. 61 (2013) 6132.
[26] P. Jacques, E. Girault, T. Catlin, N. Geerlofs, T. Kop, S. van der Zwaag, F. Delannay, Mater. Sci. Eng. A 273–275 (1999) 475.
[27] M. De Meyer, D. Vanderschueren, B. De Cooman, ISIJ Int. 39 (1999) 913.
[28] S. Traint, A. Pichler, K. Hauzenberger, P. Stiaszny, E. Werner, Steel Res. 73 (2002) 259.
[29] P.J. Jacques, Curr. Opin. Solid State Mater. Sci. 8 (2004) 259.
[30] S. Zaefferer, J. Ohlert, W. Bleck, Acta Mater. 52 (2004) 2765.
[31] D. Raabe, D. Ponge, O. Dmitrieva, B. Sander, Adv. Eng. Mater. 11 (2009) 547.
[32] N. Nakada, R. Fukagawa, T. Tsuchiyama, S. Takaki, D. Ponge, D. Raabe, ISIJ Int. 53 (2013) 1286.
[33] N. Nakada, T. Tsuchiyama, S. Takaki, D. Ponge, D. Raabe, ISIJ Int. 53 (2013) 2275.
[34] S. Lee, S.-J. Lee, B.C. De Cooman, Scr. Mater. 65 (2011) 225.
[35] A. Arlazarov, M. Gouné, O. Bouaziz, A. Hazotte, G. Petitgand, P. Barges, Mater. Sci. Eng. A 542 (2012) 31.
[36] E. De Moor, D.K. Matlock, J.G. Speer, M.J. Merwin, Scr. Mater. 64 (2011) 185.
[37] O. Dmitrieva, D. Ponge, G. Inden, J. Millán, P. Choi, J. Sietsma, D. Raabe, Acta Mater. 59 (2011) 364.
[38] F. Moszner, A.S. Sologubenko, M. Schinhammer, C. Lerchbacher, A.C. Hänzi, H. Leitner, P.J. Uggowitzer, J.F. Löffler, Acta Mater. 59 (2011) 981.
[39] B. Hutchinson, J. Hagström, O. Karlsson, D. Lindell, M. Tornberg, F. Lindberg, M. Thuvander, Acta Mater. 59 (2011) 5845.
[40] F. Moszner, S.S.A. Gerstl, P.J. Uggowitzer, J.F. Loeffler. Acta Mater. 2014 accepted.
[41] M.-M. Wang, C.C. Tasan, D. Ponge, A. Kostka, D. Raabe, Acta Mater. 79 (2014) 268.
[42] A.P. Hammersley, S.O. Svensson, M. Hanfland, A.N. Fitch, D. Häusermann, High Press. Res. 14 (1996) 235.
[43] L. Velterop, R. Delhez, T.H. de Keijser, E.J. Mittemeijer, D. Reefman, J. Appl. Crystallogr. 33 (2000) 296.
[44] T. Shintani, Y. Murata, Acta Mater. 59 (2011) 4314.
[45] C.A. Schneider, W.S. Rasband, K.W. Eliceiri, Nat. Methods 9 (2012) 671.
[46] M.D. Abràmoff, P.J. Magalhães, S.J. Ram, Biophotonics Int. 11 (2004) 36.
[47] B. Fultz, J.W. Morris, Metall. Trans. A 16A (1985) 2251.
[48] J.I. Kim, H.J.A.E. Kim, J.W. Morris, Metall. Trans. A 15A (1984) 2213.
[49] P.J. Jacques, Q. Furnémont, F. Lani, T. Pardoen, F. Delannay, Acta Mater. 55 (2007) 3681.
[50] M. Hoelscher, D. Raabe, K. Luecke, Acta Metall. Mater. 42 (1994) 879.
[51] D. Raabe, M. Hoelscher, M. Dubke, K.-H. Hanke, H. Pfelfer, K. Luecke, Steel Res. 64 (1993) 359.
[52] E. Orowan, Symp. Intern. Stress Inst. Met. London 451 (1947).
[53] R.F. Decker, J.T. Eash, A.J. Goldman, Trans. ASM 55 (1962).
[54] W. Sha, A. Cerezo, A.S. Company, U. States, Mater. A 24 (1993) 1233.
[55] C. Servant, N. Bouzid, Acta Metall. 36 (1988) 2771.
[56] V.K. Vasudevan, S.J. Kim, C.M. Wayman, Metall. Trans. A 21 (1990).
[57] R. Tewari, S. Mazumder, I.S. Batra, G.K. Dey, S. Banerjee, Acta Mater. 48 (2000) 1187.
[58] R.F. Decker, Source Book on Maraging Steels, ASM, Metals Park, OH, 1979.
[59] Y. Tomota, H. Tokuda, Y. Adachi, M. Wakita, N. Minakawa, A. Moriai, et al., Acta Mater. 52 (2004) 5737.
[60] S. Morito, H. Tanaka, R. Konishi, T. Furuhara, T. Maki, Acta Mater. 51 (2003) 1789.
[61] X.Z. Zhang, J.F. Knott, Acta Mater. 47 (1999) 3483.
[62] M.X. Zhang, P.M. Kelly, J. Mater. Sci. 37 (2002) 3603.
[63] B. Hwang, T.-H. Lee, S.-J. Park, C.-S. Oh, S.-J. Kim, Mater. Sci. Eng. A 528 (2011) 7257.
[64] R. Wu, W. Li, S. Zhou, Y. Zhong, L. Wang, X. Jin, Metall. Mater. Trans. A (2013).
[65] A. Markfeld, A. Rosen, Mater. Sci. Eng. 46 (1980) 151.
[66] I.B. Timokhina, P.D. Hodgson, E.V. Pereloma, Metall. Mater. Trans. A 35 (2004) 2331.
[67] R. Schnitzer, G.A. Zickler, E. Lach, H. Clemens, S. Zinner, T. Lippmann, H. Leitner, Mater. Sci. Eng. A 527 (2010) 2065.
[68] W. Zhou, H. Guo, Z. Xie, X. Wang, C. Shang, Mater. Sci. Eng. A 587 (2013) 365.

[69] R.D.K. Misra, P. Venkatsurya, K.M. Wu, L.P. Karjalainen, Mater. Sci. Eng. A 560 (2013) 693.
[70] X.D. Wang, Z.H. Guo, Y.H. Rong, Mater. Sci. Eng. A 529 (2011) 35.
[71] K. Zhang, M. Zhang, Z. Guo, N. Chen, Y. Rong, Mater. Sci. Eng. A 528 (2011) 8486.
[72] C. Herrera, D. Ponge, D. Raabe, Acta Mater. 59 (2011) 4653.
[73] X. Sun, K.S. Choi, A. Soulami, W.N. Liu, M.A. Khaleel, Mater. Sci. Eng. A 526 (2009) 140.
[74] J. Kadkhodapour, A. Butz, S. Ziaei Rad, Acta Mater. 59 (2011) 2575.
[75] S.-H. Choi, E.-Y. Kim, W. Woo, S.H. Han, J.H. Kwak, Int. J. Plast. 45 (2013) 85.
[76] C.C. Tasan, J.P.M. Hoefnagels, M.G.D. Geers, Scr Mater. 62 (2010) 835.
[77] K.S. Choi, W.N. Liu, X. Sun, M.A. Khaleel, Metall. Mater. Trans. A 40 (2009) 796.
[78] P.J. Gibbs, B.C. De Cooman, D.W. Brown, B. Clausen, J.G. Schroth, M.J. Merwin, D.K. Matlock, Mater. Sci. Eng. A (2014).
[79] S. Lee, S.-J. Lee, S. Santhosh Kumar, K. Lee, B.C.D. Cooman, Metall. Mater. Trans. A 42 (2011) 3638.
[80] F.G. Caballero, H.K.D.H. Bhadeshia, Curr. Opin. Solid State Mater. Sci. 8 (2004) 251.
[81] S.S. Babu, S. Vogel, C. Garcia-Mateo, B. Clausen, L. Morales-Rivas, F.G. Caballero, Scr. Mater. 69 (2013) 777.
[82] Y.J. Li, P. Choi, C. Borchers, S. Westerkamp, S. Goto, D. Raabe, R. Kirchheim, Acta Mater. 59 (2011) 3965.
[83] Y.J. Li, P. Choi, S. Goto, C. Borchers, D. Raabe, R. Kirchheim, Acta Mater. 60 (2012) 4005.